

# Polarimetric imaging and retrieval of target polarization characteristics in underwater environment

YALONG GU,<sup>1,2</sup> CARLOS CARRIZO,<sup>1</sup> ALEXANDER A. GILERSON,<sup>1,\*</sup> PARRISH C. BRADY,<sup>3</sup> MOLLY E. CUMMINGS,<sup>3</sup> MICHAEL S. TWARDOWSKI,<sup>4</sup> JAMES M. SULLIVAN,<sup>4</sup> AMIR I. IBRAHIM,<sup>1,5,6</sup> AND GEORGE W. KATTAWAR<sup>7</sup>

<sup>1</sup>Optical Remote Sensing Laboratory, The City College of the City University of New York, New York, New York 10031, USA

<sup>2</sup>Earth Resources Technology, Inc., Laurel, Maryland 20707, USA

<sup>3</sup>Section of Integrative Biology, University of Texas, Austin, Texas 78712, USA

<sup>4</sup>Harbor Branch Oceanographic Institute, Fort Pierce, Florida 34946, USA

<sup>5</sup>Universities Space Research Association, Columbia, Maryland 21044, USA

<sup>6</sup>NASA Goddard Space Flight Center, Greenbelt, Maryland 20771, USA

<sup>7</sup>Department of Physics and Astronomy, Texas A&M University, College Station, Texas 77843-4242, USA

\*Corresponding author: gilerson@ccny.cuny.edu

Received 21 September 2015; revised 9 December 2015; accepted 15 December 2015; posted 16 December 2015 (Doc. ID 250455); published 20 January 2016

Polarized light fields contain more information than simple irradiance and such capabilities provide an advanced tool for underwater imaging. The concept of the beam spread function (BSF) for analysis of scalar underwater imaging was extended to a polarized BSF which considers polarization. The following studies of the polarized BSF in an underwater environment through Monte Carlo simulations and experiments led to a simplified underwater polarimetric imaging model. With the knowledge acquired in the analysis of the polarimetric imaging formation process of a manmade underwater target with known polarization properties, a method to extract the inherent optical properties of the water and to retrieve polarization characteristics of the target was explored. The proposed method for retrieval of underwater target polarization characteristics should contribute to future efforts to reveal the underlying mechanism of polarization camouflage possessed by marine animals and finally to generalize guidelines for creating engineered surfaces capable of similar polarization camouflage abilities in an underwater environment. © 2016 Optical Society of America

**OCIS codes:** (010.4455) Oceanic propagation; (110.0113) Imaging through turbid media; (110.5405) Polarimetric imaging.

<http://dx.doi.org/10.1364/AO.55.000626>

## 1. INTRODUCTION

The ocean is a highly scattering and absorbing medium. Attenuation of light due to absorption and scattering by water molecules, dissolved organic and inorganic matter, and various types of suspended particles severely degrades an image in an underwater environment. However, such complex light propagation also results in partially polarized underwater light fields [1]. As polarization contains more information than irradiance, marine animals capable of polarization vision can detect underwater objects that have similar irradiance but different polarization features with respect to the background [2–4]. Due to the lack of objects for hiding, marine animals have had to evolve sophisticated strategies to cloak themselves in this highly scattering open ocean environment [5]. It was discovered recently that certain types of fish exhibit reduced polarization contrast, suggesting promising polaro-crypsis in the open ocean [6,7].

Further efforts to reveal the underlying mechanism of polaro-crypsis requires the polarization of the light field to be reflected off the fish skin in a particular way [8]. It can be also envisioned that similar features will be incorporated in a new generation of metamaterials capable of automatically displaying the same color, intensity, and polarization as the background, which should be assessed in underwater operations [9]. Although it is convenient to record polarization images of an underwater target by a video polarimeter in turbid waters [6], determining polarization of the light field leaving the target surface from its polarimetric image is not straightforward. Under natural illumination, light that is scattered by particles distributed in between the target and the imaging device (known as veiling light or path radiance) appears in the formed target image [10]. It usually has polarization characteristics that are very different from the ones of the target. This property has been

applied in the polarization filtering technique to improve target visibility and to enhance target detection in an underwater environment [11–13]. To characterize quantitatively polarization features of the target, veiling light polarization must be quantified before retrieval of target polarization. In addition, light reflected from the target surface undergoes scattering during propagation to the imaging device. As scattering induces polarization change, this factor also complicates the formed polarimetric image.

Retrieval of target polarization characteristics from its polarimetric image can be categorized as an inverse problem. Prior knowledge acquired in forward process, namely polarimetric image formation, is a key to solve this problem. One effective tool for analysis of underwater image formation is the point spread function (PSF) or its mathematical equivalent the beam spread function (BSF) [14,15]. Several empirical or simplified PSF models have been reported in the past decades [16–19]. A comparison study between these models shows that it is sufficient to model PSF by the parameters that characterize the water's optical properties [19]. Recently, a new analytical solution of 3D BSF was developed, which improved the computational simplicity and efficacy over the existing BSF models [20].

So far, most studies on PSFs in an underwater environment have focused on the scalar nature where polarization is not considered. In this paper, we extended the concept of BSF to the polarized BSF used for polarized light. The following studies of the polarized BSF through Monte Carlo simulations and experiments in laboratory conditions led to a simplified underwater polarimetric imaging model. We then analyzed polarimetric images of manmade underwater targets with known polarization properties recorded by polarimetric imaging devices in the laboratory and during a recent field trip. With knowledge acquired in the analysis of such a forward polarimetric imaging process, a method to extract the inherent optical properties of the water and finally to retrieve target polarization characteristics was explored.

The paper is organized as follows. The instruments and numerical model used throughout the whole paper are described in Section 2. The polarized BSF is defined and then studied by both Monte Carlo simulations and laboratory experiment in Section 3. Analysis of targets' polarimetric images by a simplified underwater polarimetric imaging model is presented in Section 4. A retrieval method for target polarization is investigated in Section 5. Conclusions and future work are given in Section 6.

## 2. INSTRUMENTATION AND NUMERICAL RADIATIVE TRANSFER MODEL

### A. Instruments for Laboratory and Field Experiments

In laboratory and field experiments, most of the polarization images of targets were recorded by a full Stokes vector imaging camera developed by Bossa Nova Technologies (Bossa Nova camera). This camera allows a full Stokes polarization analysis for each pixel of the image in real time. The resolution of the camera CCD is  $1040 \times 1040$  pixels and the polarization frame rate is 15 frames/second if operating in video mode [21]. During the experiment the camera was placed in an underwater housing. Design of the housing port (window) shape and

material selection were discussed in previous studies for consideration of avoiding artifacts in the generated polarization images [12]. It is known that a light ray refracts twice on passing through a flat port. The different refractive indices of water, port material and air in the housing distort the polarization of the incident ray according to the Fresnel equations for refraction ([22], Chap. 25). However, estimations and preliminary measurements of these effects in the laboratory, using a calibrated light source, showed minimal impact of this effect for typical viewing angles. The camera uses a wide-angle lens ( $F/1.2$ , focusing range 0.3 m to infinity) which gives a large depth of field and, in turn, limits the necessity of focus adjustments.

Another full Stokes vector video polarimeter constructed at the University of Texas at Austin (UT polarimeter) was also used in field experiments. The instrument employs a commercial video camera and electronically controlled birefringent wave plates for the acquisition of Stokes vector images. Details of this instrument were reported in Brady *et al.* [6].

In laboratory and field experiments, the attenuation and absorption coefficients,  $c$  and  $a$ , were measured hyperspectrally in the visible spectrum using an ac-s instrument (WET Labs). In field experiments, the volume scattering function (VSF) was measured by the Multi-Angle Scattering Optical Tool (MASCOT) developed by WET Labs. It measures the VSF for monochromatic light (658 nm) between  $10^\circ$  and  $170^\circ$  at  $10^\circ$  intervals [23].

### B. Numerical Radiative Transfer Model

The underwater polarized radiance field was also modeled by a Monte Carlo radiative transfer approach for simulation of underwater polarimetric imaging and then comparison with camera measurements. The RayXP software [24] is selected to facilitate such simulations. In the program, the atmosphere-ocean system is modeled as a multiple plane-parallel layer structure, including the atmosphere, the air-water interface, and the ocean (optically deep) layers. For a given set of parameters that characterize the molecular, aerosol, or hydrosol properties in these layers, an underwater polarized radiance field is obtained through solving the vector radiative transfer equation. These parameters can be obtained by various instruments: for example, the volume scattering function is measured by MASCOT (WET Labs) and the absorption and attenuation coefficients are measured by WET Labs ac-s instrument. More details of the numerical model using RayXP were provided before [25], but for shallow water stations.

## 3. POLARIZED BSF OF POLARIZED LIGHT IN UNDERWATER ENVIRONMENT

### A. Definition of the Polarized BSF

The PSF describes how light emitted by a point source spreads on propagation through a turbid medium, characterizing multiple scattering effects [26]. It is mathematically defined as the apparent normalized radiance of an unresolved Lambertian source (Fig. 1 left). If the unresolved Lambertian source is replaced by a collimated narrow beam placed at the center of a sphere, the BSF is defined as the generated irradiance distribution on the sphere's inner surface (Fig. 1 right). Because of the

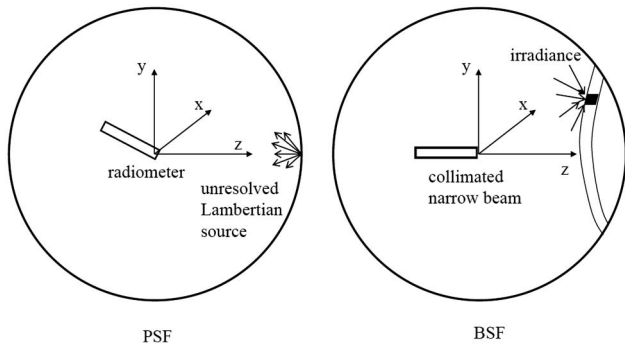


**Fig. 1.** Illustration of the definitions of the PSF (left) and BSF (right). For the PSF, an unresolved Lambertian source is placed at  $(0, 0, R)$ , the angular distribution of the radiance at the sphere center  $(0, 0, 0)$  is measured by a radiometer at  $(0, 0, 0)$ . For the BSF, a collimated narrow beam is placed on the sphere center  $(0, 0, 0)$  and the initial direction of the emitted beam is along the  $z$ -axis. The irradiance is measured on the inner surface of the sphere.

time-independent reciprocity of the electromagnetic field propagation, the PSF and BSF are mathematically equivalent [9].

Light polarization is usually characterized by the Stokes vector  $\mathbf{S} = (S_0, S_1, S_2, S_3)^T$ , where  $S_0$  represents the light radiance,  $S_1$  and  $S_2$  correspond to the linear polarization states along the parallel-perpendicular and  $\pm 45^\circ$  directions, and  $S_3$  corresponds to the circular polarization states [22]. Here,  $T$  denotes matrix transpose. From the Stokes vector, the degree of linear polarization (DoLP), a parameter indicating the magnitude of linear polarization of a light field, is defined as

$$\text{DoLP} = \frac{\sqrt{S_1^2 + S_2^2}}{S_0}. \quad (1)$$

The angle of linear polarization (AoLP) can be also computed from the Stokes vector:

$$\text{AoLP} = \frac{1}{2} \tan^{-1} \frac{S_2}{S_1}. \quad (2)$$

In this paper, the AoLP is defined between  $0^\circ$  and  $180^\circ$  [27]. In a turbid medium, the polarization of a propagating light field usually changes due to multiple scattering. The new Stokes vector is connected to the initial Stokes vector through a  $4 \times 4$  matrix known as the Mueller matrix. Therefore, one way to characterize the effect of turbid waters on polarimetric imaging systems is the so-called point spread matrix (PSM) [28]. It contains  $4 \times 4$  elements and can be determined using effective Mueller matrix calculated based on the water absorption and scattering properties on the assumption that light propagates mostly close to the  $z$  axis. Thus, the PSM is represented from the perspective of a turbid medium to model polarization change associated with underwater light propagation. This physical process can also be modeled from the perspective of an imaging system in a way similar to the PSF or BSF used in unpolarized imaging, represented by the Stokes vector. Generally, extension of the concept of both PSF and BSF for polarized light is not straightforward. For the PSF, unresolved Lambertian source is always unpolarized. For the BSF,

although an arbitrary polarization state can be assigned to a collimated narrow beam, there is no polarized irradiance. The Stokes vector is defined by spatial coordinates spanned by the light propagation direction and the associated transverse plane. As illustrated in Fig. 1 (right), irradiance is an integration of the incident radiances whose directions fall in a given solid angle. Apparently the Stokes vectors of these individual radiances are defined in different spatial coordinates. They cannot be transformed to the same coordinates by simply using the so-called rotational matrix because it describes rotation of spatial coordinates around the radiance's propagating axis [29].

However, it should be noted that determination of light polarization strongly depends on the optical setup of a measurement system. Division of time is a typical measurement principle of imaging polarimetry [30]. Both the Bossa Nova camera and the UT polarimeter used in the paper are based on this principle. A telecentric optical system is often adopted for such a measurement system [31]. As illustrated in Fig. 2, the emitted radiances on the object plane are collimated after passing through the objective lens (L1) and finally are focused on the imaging plane by a tube lens (L2). The polarization of the radiances collected by the objective lens is analyzed by recording irradiance on the imaging plane with different phase retardances introduced by two liquid crystal variable retarders. At least four measurements are required to determine the Stokes vector. From Fig. 2, it can be clearly seen that the polarization is measured in the region between the two lenses where the radiances are parallel, referred to as the collimated region. Considering that the light field in an underwater environment with natural illumination is incoherent, the Stokes vector of the collected radiances is the superposition of their own Stokes vectors after rotating to the global spatial coordinates of the collimated region.

Upon solving the issue of polarization and irradiance, the polarized BSF is defined as the distribution of the Stokes vector of a light field on a receiver plane generated by a collimated narrow beam with a given Stokes vector and unit power. Since polarimetric imaging systems usually use the Stokes vector  $\mathbf{S} = (S_0, S_1, S_2, S_3)^T$  to describe its image, the polarized BSF is correspondingly a collection of four components,

$$\text{pBSF}(\mathbf{r}, L) = (\text{pBSF}_0, \text{pBSF}_1, \text{pBSF}_2, \text{pBSF}_3)^T, \quad (3)$$

where  $\mathbf{r} = (x, y)$  denotes spatial location on the receiver plane and  $L$  is the distance between the receiver plane and the source plane. It should be noted that the four components of the polarized BSF characterize the spatial distribution of the four

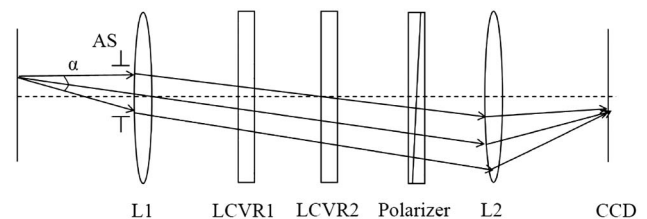


**Fig. 2.** Illustration of optical setup for imaging polarimetry. AS, aperture stop;  $\alpha$  is the angle of the aperture stop seen from the object plane (angular aperture); L1, objective lens; L2, tube lens; LCVR, liquid crystal variable retarder.

Stokes vector components on the receiver plane, respectively. They are expressed in the form of Eq. (3) just for analogy with the Stokes vector expression. For a given location on the receiver plane, Eq. (3) reduces to the Stokes vector of the light field at that location. Because the shape of a camera's image sensor is usually planar, the polarized BSF is defined on a plane, rather than on a sphere shown in Fig. 1. In principle, a collimated beam with a given polarization state should have its own polarized BSF. However, the light field in an underwater environment with natural illumination is incoherent. By the principle of additivity ([22], Chap. 4), the Stokes vector of an incoherent light field can be decomposed into a linear superposition of seven basic states:  $(1, 0, 0, 0)^T$ ,  $(1, 1, 0, 0)^T$ ,  $(1, -1, 0, 0)^T$ ,  $(1, 0, 1, 0)^T$ ,  $(1, 0, -1, 0)^T$ ,  $(1, 0, 0, 1)^T$ , and  $(1, 0, 0, -1)^T$ . This suggests that if the polarized BSFs of these seven basic polarization states are known, the polarized BSF of a collimated beam with an arbitrary polarization state can be generated by an addition of these.

**B. Monte Carlo Simulation of the Polarized BSF**

Light propagation in a turbid medium is modeled by radiative transfer theory. Under certain circumstances, the scalar PSF can be obtained by using small angle scattering approximation [32]. However, it is difficult to analytically study the polarized BSF by vector radiative transfer theory. The Monte Carlo technique, also based on radiative transfer theory, is applicable for simulating light propagation in a turbid medium under various scattering conditions. In this paper, we adopted the Monte Carlo simulation methods [24,33,34] to numerically investigate the polarized BSFs in an underwater environment. The geometry of the simulation is similar to Fig. 1 (right), except for the planar detector plane. A collimated narrow beam is placed at  $(0, 0, 0)$  and its initial direction is horizontal (along the  $z$ -axis). The detector is a square that is composed of a square pixel array. The initial power of the source is 1 in arbitrary unit.

An important step of Monte Carlo simulation is selecting an appropriate Mueller matrix to model scattering of polarized light. Measurements of Mueller matrices for oceanic waters are limited. A measurement by Voss and Fry in Atlantic waters shows that the Mueller matrix is similar to the Mueller matrix of Rayleigh scattering [35]. The reduced form is given by the following form [36],

$$M_{\text{Rayleigh}} = \begin{bmatrix} 1 & -\frac{(\sin \psi)^2}{1+(\cos \psi)^2} & 0 & 0 \\ -\frac{(\sin \psi)^2}{1+(\cos \psi)^2} & 1 & 0 & 0 \\ 0 & 0 & \frac{2 \cos \psi}{1+(\cos \psi)^2} & 0 \\ 0 & 0 & 0 & \frac{2 \cos \psi}{1+(\cos \psi)^2} \end{bmatrix}, \tag{4}$$

where  $\psi$  is the scattering angle. The phase function of the ocean is taken to be the Henyey–Greenstein phase function [36]:

$$\tilde{\beta}(\psi, g) = \frac{1}{4\pi} \frac{1 - g^2}{(1 + g^2 - 2g \cos \psi)^{3/2}}. \tag{5}$$

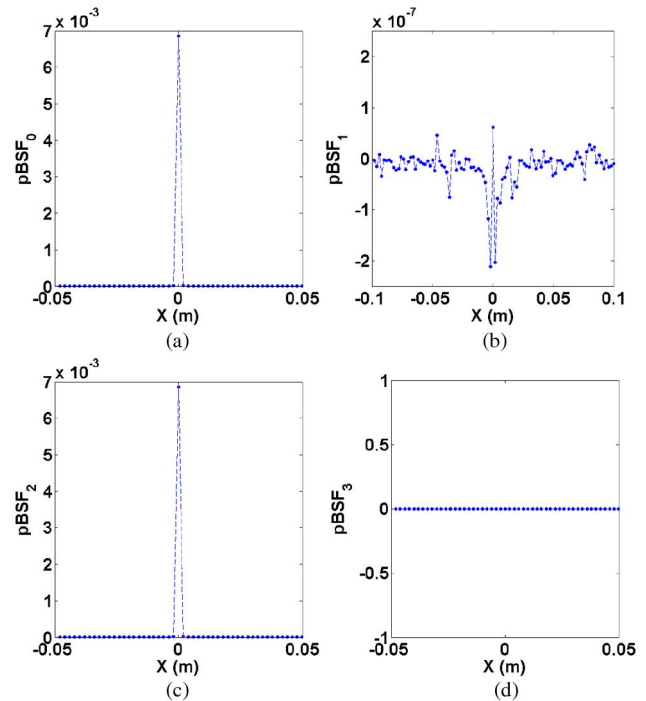
Here, the parameter  $g$  is a measure of the relative amounts of forward and backward scattering. The Mueller matrix that models polarization modulation of light scattering in the ocean is taken to be in the following form [37],

$$M = b\tilde{\beta}(\psi, g)M_{\text{Rayleigh}}, \tag{6}$$

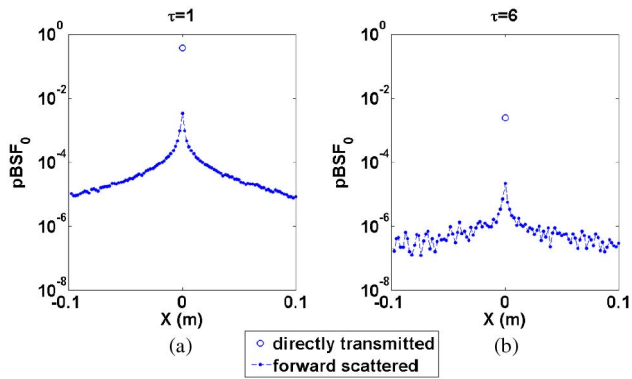
where  $b$  is the scattering coefficient. It is connected to the attenuation coefficient  $c$  via the relationship  $b = \omega_0 c$ , where  $\omega_0$  is the single scattering albedo.

Figure 3 shows the four components of the polarized BSF of a collimated point source whose initial Stokes vector is  $(1, 0, 1, 0)^T$ . It can be seen that the  $\text{pBSF}_0$  and  $\text{pBSF}_2$  components are almost the same. Their power is of the order of  $10^{-3}$ . The multiple scattering processes induce coupling between the individual components of the Stokes vector. Although  $\text{pBSF}_3 = 0$ ,  $\text{pBSF}_1$  is nonzero, but is much less than  $\text{pBSF}_0$  and  $\text{pBSF}_2$ . It suggests that on propagation in such a forward scattering medium, the polarization state can be maintained while the image is blurred. Simulation shows that the polarized BSFs of other basic polarization states also exhibit the same feature. For example,  $\text{pBSF}_0$  and  $\text{pBSF}_1$  are almost the same for  $(1, 1, 0, 0)^T$  while  $\text{pBSF}_2$  is very small and  $\text{pBSF}_3 = 0$ .

On propagation in a turbid medium, the light received by a detector is composed of two parts, the directly transmitted light (nonscattered) and the forward scattered light. While the former follows the Bouguer's law (also known as the Bouguer–Lambert–Beer law), the latter's characterization is complex. However, the peak of the  $\text{BSF}_0$  component shown in Fig. 3 is  $6.9 \times 10^{-3}$ , which is very close to  $e^{-5}$  predicted by the Bouguer's law. It means that the directly transmitted part is the dominant component. This is not surprising as scattering events are rare when the optical thickness is small and then the



**Fig. 3.** Polarized BSF in the observation plane. The Stokes vector of the point source is  $(1, 0, 1, 0)^T$ . The parameter  $g$  in the Henyey–Greenstein phase function is taken to be 0.9. The attenuation coefficient  $c$  is  $1 \text{ m}^{-1}$ . The distance between the source and the observation plane is 5 m, so the optical thickness  $\tau = cL$  is 5. The single scattering albedo is 0.8. The pixel size of the observation plane is 2 mm. The unit of the polarized BSF is power.



**Fig. 4.** Directly transmitted and forward scattered parts for the  $\text{pBSF}_0$  component, obtained by Monte Carlo simulation. The optical thicknesses are 1 and 6, respectively. The Stokes vector of the initial collimated source is  $(1, 1, 0, 0)^T$ . The rest of the parameters are the same as in Fig. 3.

collected forward scattered light is weak. When the optical thickness is sufficiently large, the dominant part of the received light is the forward scattered part. The optical thickness at which the transition occurs depends on the attenuation coefficient. It was reported that when  $c = 1 \text{ m}^{-1}$  this optical thickness is between 10 and 20 [38]. Figure 4 shows a comparison between the directly transmitted and the forward scattered parts for the  $\text{pBSF}_0$  component, obtained by Monte Carlo simulation. It can be seen that the magnitude of the directly transmitted light is much higher than the central peak of the forward scattered light when the optical thickness is small or moderate. Under such circumstances, the polarized BSF can be simplified to the following form,

$$\text{pBSF}(\mathbf{r}, z) = \mathbf{S}_{\text{source}}(\mathbf{r}_0)\delta(\mathbf{r} - \mathbf{r}_0)\exp(-cL), \quad (7)$$

where  $\mathbf{S}_{\text{source}}$  is the Stokes vector of the collimated narrow source beam and  $\mathbf{r}_0$  indicates the location of the beam on the source plane,  $\delta(\mathbf{r})$  is the Dirac function.

### C. Laboratory Experiment of Polarized Light Propagation through Turbid Water

The Monte Carlo simulations shown in Section 3.B suggest that a polarized light field can maintain its polarization properties on passing through turbid water with a relatively small optical thickness. This prediction was verified by a laboratory experiment. The experimental setup is illustrated in Fig. 5. An integrating sphere (OL-455-8-1, Optronics Laboratories, FL) emitted a uniform radiance light field across the output port which is similar to the conditions in water in the horizontal direction. After passing through a  $0^\circ$  linear polarizer positioned in an optical mount, a fully linear polarized light field was generated and then propagated through a water tank whose length is 0.5 m. The Bossa Nova camera was used to measure the Stokes vector of the transmitted light on the other side of the tank. Because the polarization was measured by recording of an image of the light footprint, the camera was focused on the left side of the tank. The tank was filled at first with tap water. The water turbidity was changed by adding antacid

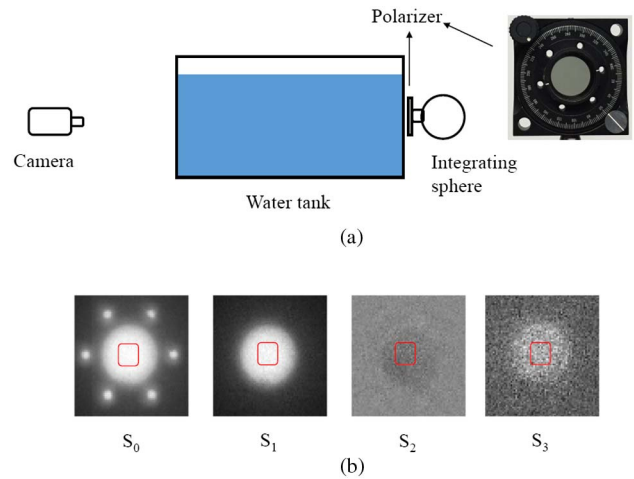


**Fig. 5.** (a) Illustration of the experiment setup for polarization measurement of the light after passing through the water tank. (b) The full Stokes vector image of a measurement. For the purpose of display, the range of gray values is different in these gray-scale images. The magnitude of  $S_2$  and  $S_3$  is much smaller than  $S_0$  and  $S_1$ .

liquid distributed by CVS Pharmacy, Inc (an alternative of Maalox antacid). The attenuation coefficient of the turbid water at the wavelength of 530 nm was measured by an acs-instrument (WET Labs). The camera operated in the green band centered at 530 nm in the experiment. The total number of measurements is nine, each with different turbidity conditions. The full Stokes vector image of a measurement is shown in Fig. 5(b). The patterns of  $S_0$  and  $S_1$  are rather uniform, but the patterns of  $S_2$  and  $S_3$  are random. Six small spots in the  $S_0$  image correspond to the small holes on the mount. Because they were not covered by the polarizer and the illuminating light field from the integrating sphere was unpolarized, they are absent in  $S_1$ ,  $S_2$ , and  $S_3$  images.

When we used the software associated with the Bossa Nova camera to monitor real-time polarization image, fluctuations of the image's Stokes vectors were observed. For each measurement, a snapshot of the polarization image was recorded. We selected the central area [indicated by red squares in Fig. 5(b)] of the full Stokes images and with assumption of ergodicity, used the characteristics of the pixels' Stokes vectors in this area to analyze the measurement results. The measurement uncertainties were evaluated through the standard deviations (STDs) of the selected pixels' Stokes vectors and corresponding DoLPs and AoLPs. The analysis is presented in Fig. 6, as a function of the optical thickness  $cL$ . Similar to the polarized light incident on the water tank's right side, the propagated light field has negligible  $S_2$  and  $S_3$  components compared to the  $S_0$  [Fig. 6(b)] and almost invariant AoLP close to  $0^\circ$  [Fig. 6(d)]. The STDs of  $S_2$  and  $S_3$  are also negligible when they are normalized to  $S_0$ . The STDs of AoLP are less than  $0.7^\circ$ . Both the  $S_0$  and  $S_1$  components of the propagated light on the left side of the water tank followed an exponential decay as the water became more and more turbid. The decay rate is close to the attenuation coefficient  $c$  predicted by the Bouguer's law [shown as the  $-1:1$  line in Fig. 6(a)] at the beginning. However, it gradually deviates from  $-1:1$  line with increased

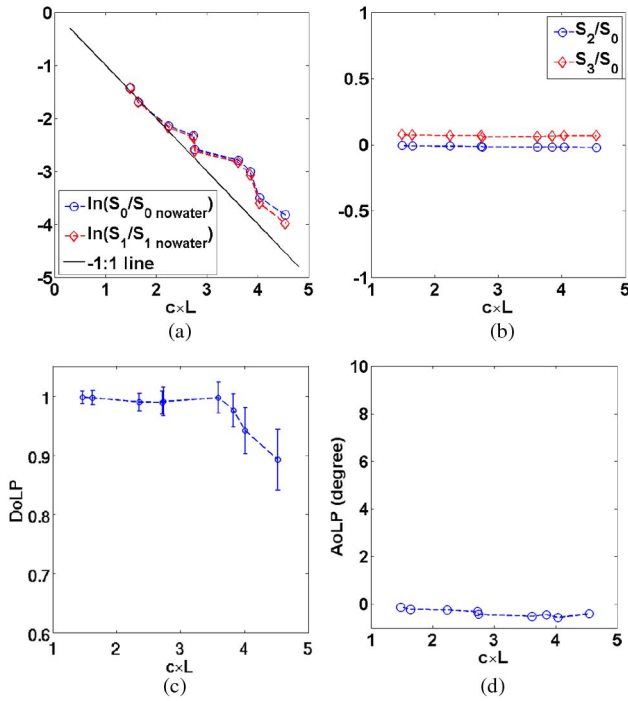


**Fig. 6.** Measured Stokes vector of transmitted light on the left side of the water tank and the corresponding DoLP and AoLP. The  $-1:1$  line in (a) shows the exponential decay at the rate of the attenuation coefficient  $c$  predicted by the Bouguer's law. DoLP and AoLP are the means of the pixels' DoLPs and AoLPs inside the selected area. Because errors of  $\ln(\frac{S_0}{S_{0\text{nowater}}})$ ,  $\ln(\frac{S_1}{S_{1\text{nowater}}})$ ,  $\frac{S_2}{S_0}$ ,  $\frac{S_3}{S_0}$ , and AoLP are negligible, only error bars of DoLP are shown in Fig. 6(c).

water turbidity. The measured DoLP is close to 100% when water turbidity is low, agreeing with the Monte Carlo simulations in Section 2.B. It decreases when  $c \times L > 3.5$ , roughly at the similar water turbidity where the measured decay rate of the  $S_0$  and  $S_1$  components deviates from the attenuation coefficient  $c$ . With such water turbidity, the transmitted light signal was weak and switch of the camera gain level was required, which was associated with the change of the signal-to-noise ratio. The ratio between mean and STD of both  $S_0$  and  $S_1$  increases as the water became turbid. The maximum ratio is around 6% when the water was the most turbid (the ninth measurement). However, these variations are negligible when they are normalized to  $S_{0\text{nowater}}$  and  $S_{1\text{nowater}}$ . Errors of DoLP also increase as a function of water turbidity. It should be noted that deviation of decay rate of both  $S_0$  and  $S_1$  happened when the transmitted signal was weak (considering  $e^{-3.5} \approx 0.03$ ). Further study is probably necessary for accurate measurement of such a weak signal and it requires a better calibrated instrument with higher sensitivity and larger dynamic range. It has also been reported that depolarization of polarized light is negligible over long-range propagation through fog [39]. Based on these considerations, we concluded that the slow decay rate when  $c \times L > 3.5$  shown in Fig. 6(a) and depolarization shown in Fig. 6(c) are probably due to the camera's limitations and that the propagated light has the same polarization as the incident light, as predicted by the Monte Carlo simulations.

## 4. ANALYSIS OF POLARIMETRIC IMAGE OF UNDERWATER TARGET BY FULL STOKES VECTOR IMAGING CAMERA

### A. Simplified Underwater Polarimetric Imaging Model

In an underwater environment with natural illumination, a formed scalar image  $I_{\text{image}}$  can be conceptually expressed by a convolution of the target reflectance pattern  $I_{\text{target}}$  and the underwater PSF together with the veiling light  $I_{\text{veiling}}$ :

$$I_{\text{image}} = I_{\text{target}} * \text{PSF} + I_{\text{veiling}}. \quad (8)$$

Equation (8) cannot be extended to model the polarimetric imaging process by simply replacing  $I_{\text{image}}$ ,  $I_{\text{target}}$ , and  $I_{\text{veiling}}$  with the corresponding Stokes vectors  $\mathbf{S}_{\text{image}}$ ,  $\mathbf{S}_{\text{target}}$ , and  $\mathbf{S}_{\text{veiling}}$  due to the ill-defined PSF for polarimetric imaging. However, the light field emitted by a point source can be modeled as a bundle of rays using the ray description of light. Their propagation behaviors in turbid waters are characterized by the polarized BSF considering that a collimated narrow beam can be treated as a geometric ray. The results presented in Section 3 show that the forward scattering-induced beam spreading is negligible when the optical thickness is relatively small. A collimated narrow beam decays uniformly following the Bouguer's law but maintains its initial polarization properties. Then geometric ray tracing can be used to investigate the underwater polarimetric imaging process. From Fig. 2, it can be seen that the optical setup of a polarimetric imaging camera, in particular the aperture stop, influences the measured polarization pattern of the scene. The aperture stop determines the angular range of the radiances from an object point that can be collected by the camera. In practice, the aperture stop size is much smaller than the distance between the target and the camera, meaning  $0^\circ$  angular aperture. This approximation suggests that it is sufficient to use only one ray that connects the target point and the corresponding image pixel via the center of the optical imaging system. Based on these considerations, we arrived at a simplified underwater polarimetric imaging model (illustrated in Fig. 7),

$$\mathbf{S}_{\text{image}} = \mathbf{S}_{\text{target}} \times \exp(-cL) + \mathbf{S}_{\text{veiling}}. \quad (9)$$

where  $L$  denotes the distance between the target and the camera.  $\mathbf{S}_{\text{target}}$  is the Stokes vector of radiances leaving the target

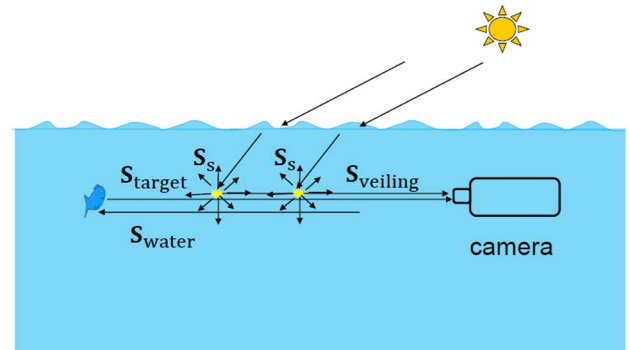


**Fig. 7.** Illustration of underwater polarimetric imaging model.  $\mathbf{S}_s$  is the Stokes vector of the underwater radiance field.  $\mathbf{S}_{\text{water}}$  and  $\mathbf{S}_{\text{veiling}}$  are calculated from  $\mathbf{S}_s$  via Eqs. (11) and (12).

surface. For a passive underwater imaging process, it is a product of the Stokes vector of underwater light incident on the target surface ( $\mathbf{S}_{\text{water}}$ ) and the Mueller matrix that characterizes polarization modulation by the target ( $M_{\text{target}}$ ):

$$\mathbf{S}_{\text{target}} = M_{\text{target}} \times \mathbf{S}_{\text{water}} \quad (10)$$

$\mathbf{S}_{\text{veiling}}$  is the Stokes vector of the veiling light, scattered light toward the camera by scatterers along the line-of-sight.

Under natural illumination, the underwater radiance whose Stokes vector is denoted by  $\mathbf{S}_s$  originates from the Sun light after absorption/scattering by aerosols in the atmosphere, refraction at the atmosphere–ocean interface, and absorption/scattering by hydrosols in the ocean. The  $S_0$  component of  $\mathbf{S}_{\text{water}}$  and  $\mathbf{S}_{\text{veiling}}$  can be calculated from the  $S_0$  component of  $\mathbf{S}_s$  by an integral  $\int S_{0s} \times \exp(-\gamma z) dz$ . The decay rate  $\gamma$  depends on both the inherent optical properties of water and measurement system parameters, for example, the optical thickness and receiver aperture. Its value is bounded in between the absorption coefficient  $a$  (large optical thickness, multiple-scattered regime) and the attenuation coefficient  $c$  (small optical thickness, nonscattered regime) [40]. Usually, it is problematic to calculate the other three components of  $\mathbf{S}_{\text{water}}$  and  $\mathbf{S}_{\text{veiling}}$  by similar integrals because for a large optical thickness the propagated light field is dominated by multiple scattered light whose polarization properties have changed. However, considering a small amount of scattered light which can be received with a small aperture of the polarization camera, the Stokes vector of the propagated light field follows the Bouguer's law even in the multiple-scattered regime [41]. Therefore  $\mathbf{S}_{\text{water}}$  and  $\mathbf{S}_{\text{veiling}}$  can be calculated from  $\mathbf{S}_s$  by an integral  $\int \mathbf{S}_s \times \exp(-cz) dz$ . In particular,  $\mathbf{S}_{\text{water}}$  was obtained by the integration from 0 to infinity,

$$\mathbf{S}_{\text{water}} = \mathbf{S}_s / c, \quad (11)$$

while  $\mathbf{S}_{\text{veiling}}$  was obtained by the integration from 0 to  $L$ :

$$\mathbf{S}_{\text{veiling}} = \frac{\mathbf{S}_s [1 - \exp(-cL)]}{c}. \quad (12)$$

The attenuation coefficient  $c$  can vary with depth but here it is considered as a constant in Eqs. (9)–(12). It should be noted that the underwater light field varies along different directions.  $\mathbf{S}_s$  represents an angular distribution of the corresponding Stokes vector in  $4\pi$  solid angle. Depending on the target–camera geometry, specific  $\mathbf{S}_s$  along an appropriate direction should be selected to calculate  $\mathbf{S}_{\text{water}}$  and  $\mathbf{S}_{\text{veiling}}$  by Eqs. (11) and (12). To illustrate, an example is shown in Fig. 7 when the surface of a target is reflective and normal to the camera, the direction of the underwater radiance  $\mathbf{S}_s$  used in Eqs. (11) and (12) for calculating  $\mathbf{S}_{\text{target}}$  is normal to the target surface,  $180^\circ$  from the direction toward the camera. If the target's reflective surface tilts with respect to the optical axis of the camera, the selected direction of the underwater radiance  $\mathbf{S}_s$  should also be tilted correspondingly according to the law of reflection.

## B. Field Experiments and Results Analysis

Polarization images of an underwater target were acquired in a field experiment in July 2012, near Curacao, Netherlands Antilles, approximately 30 m from the shore. During the experiments, both the Bossa Nova camera and target were integrated in an experimental set which was originally constructed

for polarization measurement of an underwater light field [42]. Figure 8(a) is a picture of the whole experimental setup.

The target was mounted vertically at the center of a frame while the camera (placed in housing) was positioned on one of the frame's legs 1 m away from the target in the horizontal direction. With two attached computer-controlled thrusters, the integrated target–camera system can be rotated both clockwise and counterclockwise. Such rotation changes the viewing azimuthal angle of the target with respect to the Sun [Fig. 8(c)], effectively altering the illumination conditions of the target and the water between the target and the camera. For example, the Sun is behind the target–camera system when the azimuthal angle is  $0^\circ$  and then gradually moves to the front of the target–camera system when the azimuthal angle rotates to  $180^\circ$ . The target used in field experiments [Fig. 8(b)] is a  $3 \times 3$  linear polarizer array (TECHSPEC high contrast linear polarizing film, Edmund Optics, NJ) attached on a stainless steel mirror (Mirrored Stainless Solutions, WI) by a substrate (clear cellulose, or acetate film, 0.02 in. thick, McMaster-Carr, NJ). Depolarizing film (Virgin PTFE, Fluoro-Plastics) was placed on top of the left two columns of the array. The target was imaged by the camera at different times and locations (labeled by stations). Polarimetric images presented in this section are from three stations (Stations A, B, and C). All of them were recorded at the same location ( $12^\circ 10' 38.5''$  N,  $69^\circ 1' 30.0''$  W) but at different times. In the acquired polarization images, the target only occupies the central area. The neighboring area is the image of the ocean, effectively formed by the underwater light that propagated toward the camera. Therefore, pixels outside the target were selected to evaluate the underwater light polarization measured by the camera ( $\mathbf{S}_{\text{water}}$ ). We also used simulated underwater radiance  $\mathbf{S}_s$  by RayXP to calculate the Stokes vector of the underwater light field  $\mathbf{S}_{\text{water}}$  through Eq. (11). RayXP output gave an angular distribution of  $\mathbf{S}_s$  within  $4\pi$  solid angle, indicating variant polarization of the underwater light field along different directions. The underwater radiance  $\mathbf{S}_s$  whose direction is toward the camera was used to calculate  $\mathbf{S}_{\text{water}}$ . The measured  $S_0$  component and the DoLP of the underwater light field obtained at Station A (recorded at 9:35 am, 10 July 2012) are shown in Fig. 9.

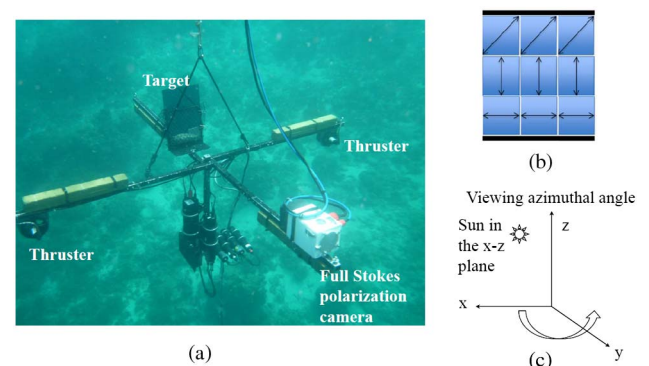


**Fig. 8.** (a) Picture of the whole experimental setup. (b) Illustration of the target. (c) Definition of viewing azimuthal angle. The double arrows indicate the orientation of the axis of the linear polarizer. The side length of each polarizer is 7 cm.

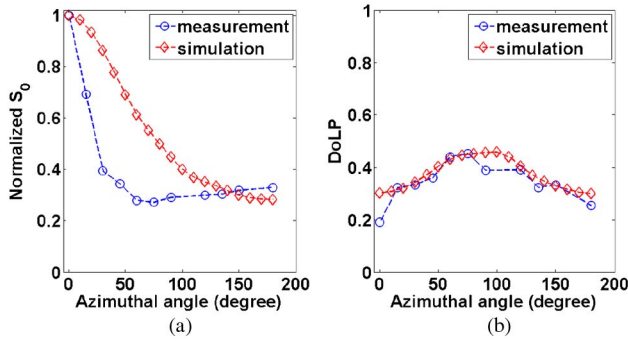


**Fig. 9.** (a)  $S_0$  component (normalized to the value at  $0^\circ$  azimuthal angle) and (b) DoLP of the underwater light  $\mathbf{S}_{\text{water}}$  measured by the polarimeter and camera and simulated by the simplified underwater polarimetric imaging model (Station A).

The attenuation coefficient measured at this station at 530 nm is  $c = 0.21 \text{ m}^{-1}$ . Because the camera axis was aligned horizontally, the direction of  $\mathbf{S}_s$  was in the horizontal plane. In Fig. 9, the  $S_0$  component is normalized to the value at  $0^\circ$  azimuthal angle due to unknown scaling relationship among the RayXP simulation and the camera measurement. In general, the match shown in Fig. 9 can be considered satisfactory taking into account variability of measurement and simulation approaches. In particular, the DoLP from the camera measurement well agrees with the DoLP from the RayXP simulation. As discussed in Section 4.A, the camera's aperture stop determines the angular range of the radiances from an object point that can be collected by the camera. Polarimetric measurements of the underwater light field show that its polarization is anisotropic, varying along different directions [42,43]. The Stokes vector of the corresponding image pixel is the superposition of the Stokes vectors of the individual radiances, resulting in reduced DoLP. However, only one ray was used in simulating  $\mathbf{S}_{\text{water}}$  by RayXP and Eq. (9). The agreement between the simulated DoLP and the measured DoLP by the camera shown in Fig. 9 suggests that the  $0^\circ$  angular aperture approximation used in the simplified underwater polarimetric imaging model Eq. (9) is valid.

The Stokes vector components of a target element measured by the camera as a function of the viewing azimuthal angle are shown in Fig. 10. The selected element is the  $90^\circ$  linear polarizer without depolarizer film [the middle of the right column in Fig. 8(b)]. The corresponding Stokes vector components were also simulated using the simplified underwater polarimetric imaging model Eq. (9). Here,  $\mathbf{S}_{\text{water}}$  and  $\mathbf{S}_{\text{veiling}}$  were calculated from RayXP simulated  $\mathbf{S}_s$  via Eqs. (11) and (12), respectively. As illustrated by Fig. 8(a),  $\mathbf{S}_{\text{veiling}}$  is an integration of the scattered light toward the camera, so the directions of these radiances  $\mathbf{S}_s$  were also toward the camera. Calculation of  $\mathbf{S}_{\text{target}}$  requires specification of the Mueller matrix  $M_{\text{target}}$  that characterizes polarization change imposed by the target. As the selected target element is a  $90^\circ$  linear polarizer attached on a stainless steel mirror by a substrate, the Mueller matrix is modeled as

$$M_{\text{target}} = \eta_{90^\circ}^2 \times \eta_{\text{substrate}}^2 \times M_{90^\circ} \times M_{\text{mirror}} \times M_{90^\circ}, \quad (13)$$

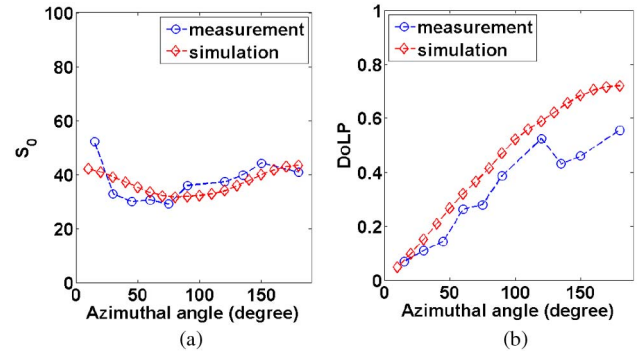


**Fig. 10.** (a)  $S_0$  component and (b) DoLP measured by the camera and simulated by the simplified underwater polarimetric imaging model for the target element  $90^\circ$  linear polarizer (Station A). Because of the unknown scaling relationship between the camera and the RayXP simulation, the simulated  $S_0$  component is rescaled.

where  $M_{90^\circ}$  and  $M_{\text{mirror}}$  are the Mueller matrices of the  $90^\circ$  linear polarizer and the mirror ([22], Chap. 5). The loss on passing through the polarizer and the substrate are characterized by the transmittance  $\eta_{90^\circ}$  and  $\eta_{\text{substrate}}$ , which are 88% and 95%, respectively. Because the reflective target surface was normal to the camera's axis and the image of the selected target element was close to the center of the whole image frame, the direction of the underwater radiance  $\mathbf{S}_s$  used in Eqs. (10), (11), and (13) for calculating  $\mathbf{S}_{\text{target}}$  was normal to the target surface,  $180^\circ$  from the direction toward the camera. The good match observed for the most azimuth angles in Fig. 10 confirms the reasonable accuracy of the simplified underwater polarimetric imaging model at least for clear waters.

The UT polarimeter was also used in the experiment. It was positioned on the same frame but on the opposite side from the target as the Bossa Nova camera. The target imaged by this instrument was the same stainless steel mirror (Mirrored Stainless Solutions, WI) but without an additional target shown in Fig. 8(b). The reflection on the mirror surface is specular. The corresponding Mueller matrix can be calculated by Fresnel's reflection equations ([22], Chap. 25). The measurement results at Station B (recorded at 10:09 am, 9 July 2012) are shown in Fig. 11. Corresponding plots by simulation are also shown. The simulation was similar to the case of the  $90^\circ$  linear polarizer shown in Fig. 10, except that  $M_{\text{target}}$  used in Eq. (10) is only the Mueller matrix of the mirror. At this station, the mirror surface was normal to the video polarimeter. It can be seen from Fig. 11 that the measured plots fluctuate, probably because the turbulent water motion made the mirror vibrate randomly, yielding unstable results. However, the simulated and measured plots of  $S_0$  and DoLP have reasonable agreement. Measurement results at Station C (recorded at 10:47 am, 9 July 9 2012) are shown in Fig. 12. At this station, the mirror surface normal was  $-30^\circ$  with respect to the video polarimeter's viewing axis. Figure 12 shows that the mirror rotation induced the shift of all plots to larger azimuthal angles. Like in Fig. 11, both  $S_0$  and the DoLP plots match reasonably well. The attenuation coefficient measured at Stations B and C is also  $c = 0.21 \text{ m}^{-1}$ .

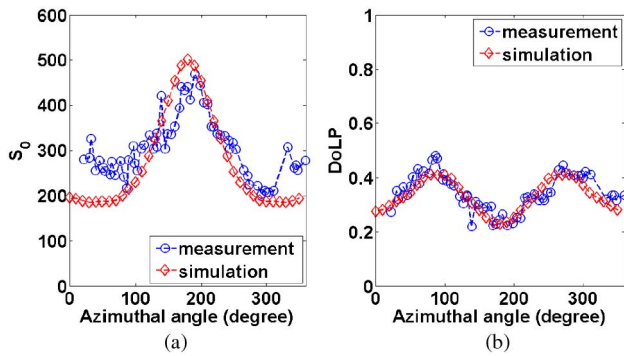


**Fig. 11.** (a)  $S_0$  component and (b) DoLP measured by the video polarimeter and simulated by the simplified underwater polarimetric imaging model for the mirror (Station B). Because of the unknown scaling relationship between the video polarimeter and the RayXP simulation, the simulated  $S_0$  component is rescaled.

## 5. RETRIEVAL OF TARGET POLARIZATION IN UNDERWATER ENVIRONMENT

In Section 4, we used a simplified underwater polarimetric imaging model to analyze the full Stokes vector polarimetric images of manmade targets in a field experiment. Analysis of experimental results shows that the polarization characteristics of a target recorded by a polarization camera can significantly change even in clear waters. As evidenced by Fig. 10(b), the polarimetric image of a  $90^\circ$  linear polarizer is not fully linearly polarized when it was taken in an underwater environment and its DoLP strongly depends on the azimuthal angle due to changes in illumination and viewing parameters and corresponding changes in proportion between the signal from the target and the veiling light. As target polarization characteristics are required for studying the underlying mechanism of polarocrypsis possessed by certain types of fish as well as other processes and objects, developing a method for polarization retrieval from an underwater target's polarimetric images is of great scientific and technological interest.

Such polarization retrieval requires solving an inverse problem, namely conversion of the polarization image of an object to the object information that generates such an image. Prior knowledge acquired in forward polarimetric image formation process is key for solving this problem. From the simplified underwater polarimetric imaging model [Eq. (9)], it is the veiling light that changes the polarization characteristics of the target image. Although both the veiling light and the light from the target contribute to the target image, they are mutually independent according to Eq. (9). This observation suggests that the Stokes vector of the veiling light can be estimated from the Stokes vector image of a target with known polarization. The target that satisfies this requirement includes  $0^\circ$ ,  $45^\circ$ ,  $90^\circ$ , and  $135^\circ$  linear polarizers. They work as polarization filters. For example, both  $0^\circ$  and  $90^\circ$  polarizers completely remove the  $S_2$  and  $S_3$  components. According to Eq. (10), the  $S_2$  and  $S_3$  components of  $\mathbf{S}_{\text{target}}$  corresponding to these two polarizers are zero. In other words, the  $S_2$  component of  $\mathbf{S}_{\text{image}}$  corresponding to  $0^\circ$  and  $90^\circ$  polarizers is only from  $\mathbf{S}_{\text{veiling}}$ . Likewise, the  $S_1$  component of  $\mathbf{S}_{\text{image}}$  corresponding to  $45^\circ$  and  $135^\circ$  polarizers is

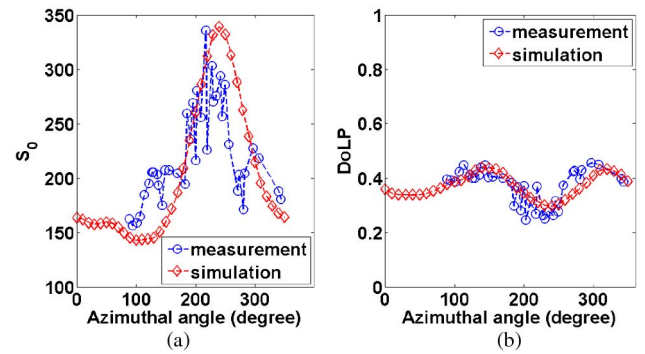


**Fig. 12.** (a)  $S_0$  component and (b) DoLP measured by the video polarimeter and simulated by the simplified underwater polarimetric imaging model for the mirror (Station C). Because of the unknown scaling relationship between the video polarimeter and the RayXP simulation, the simulated  $S_0$  component is rescaled.

only from  $\mathbf{S}_{\text{veiling}}$  as they completely remove the  $S_1$  and  $S_3$  components.

### A. Target Polarization Retrieval: Laboratory Experiment

We followed the above principle to demonstrate a polarization retrieval method through a laboratory experiment. The setup is illustrated in Fig. 13, which is similar to the setup for the experiment of polarized light propagation through turbid water shown in Fig. 5(a) except an additional desk lamp was installed above the water tank. Upon illuminating the turbid water in the tank by such a lamp, partially polarized veiling light was generated.

In the experiment, a linear polarizer was positioned on an optical rotation mount and illuminated by an integrating sphere. The polarization axis was rotated to  $0^\circ$ ,  $45^\circ$ ,  $90^\circ$ , and  $135^\circ$  positions, respectively. At each position, the polarization image was recorded by a full Stokes vector imaging camera (Boss Nova Technologies) operated in the green band centered at 530 nm. Their recorded Stokes vector images were labeled as  $\mathbf{S}_{0^\circ}$ ,  $\mathbf{S}_{45^\circ}$ ,  $\mathbf{S}_{90^\circ}$ , and  $\mathbf{S}_{135^\circ}$ , respectively. Table 1 summarizes their relationship with the veiling light's Stokes vector  $\mathbf{S}_{\text{veiling}}$ , calculated by Eqs. (9) and (10). Because circular polarization was negligible, the  $S_3$  component was not included. Then the first

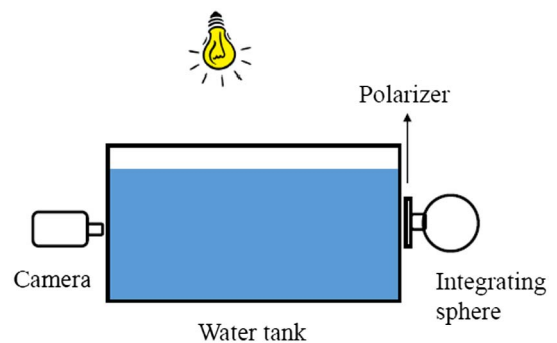


**Fig. 13.** Illustration of the setup for the laboratory experiment of target polarization retrieval. The light bulb without polarizer represents the lighting in the laboratory room.

**Table 1. Relationship between the Stokes Vector Images ( $S_{0^\circ}$ ,  $S_{45^\circ}$ ,  $S_{90^\circ}$ , and  $S_{135^\circ}$ ) and the Veiling Light's Stokes Vector  $S_{\text{veiling}}$ <sup>a</sup>**

Polarizer	Camera Measurement		
	$S_0$	$S_1$	$S_2$
$0^\circ$	$S_{0,\text{veiling}} + tS_{0,\text{IS}}$	$S_{1,\text{veiling}} + tS_{0,\text{IS}}$	$S_{2,\text{veiling}}$
$45^\circ$	$S_{0,\text{veiling}} + tS_{0,\text{IS}}$	$S_{1,\text{veiling}}$	$S_{2,\text{veiling}} + tS_{0,\text{IS}}$
$90^\circ$	$S_{0,\text{veiling}} + tS_{0,\text{IS}}$	$S_{1,\text{veiling}} - tS_{0,\text{IS}}$	$S_{2,\text{veiling}}$
$135^\circ$	$S_{0,\text{veiling}} + tS_{0,\text{IS}}$	$S_{1,\text{veiling}}$	$S_{2,\text{veiling}} - tS_{0,\text{IS}}$

<sup>a</sup> $S_{\text{IS}}$  represents the Stokes vector of the light field emitted by the integrating sphere. Because it is unpolarized,  $S_{\text{IS}} = (S_{0,\text{IS}}, 0, 0, 0)^T$ . The transmission coefficient  $t$  accounts for the total loss when the light field passes through the polarizer, the turbid water in the tank, and the tank windows.

three components of the veiling light's Stokes vector can be estimated by the following expressions:

$$S_{1,\text{veiling}} = (S_{1,45^\circ} + S_{1,135^\circ})/2, \quad (14a)$$

$$S_{2,\text{veiling}} = (S_{2,0^\circ} + S_{2,90^\circ})/2, \quad (14b)$$

$$S_{0,\text{veiling}} = \text{mean} \left\{ \begin{array}{l} S_{0,0^\circ} - (S_{1,0^\circ} - S_{1,\text{veiling}}) \\ S_{0,45^\circ} - (S_{2,45^\circ} - S_{2,\text{veiling}}) \\ S_{0,90^\circ} + (S_{1,90^\circ} - S_{1,\text{veiling}}) \\ S_{0,135^\circ} + (S_{2,135^\circ} - S_{2,\text{veiling}}) \end{array} \right\}. \quad (14c)$$

Here,  $S_{1,\text{veiling}}$  and  $S_{2,\text{veiling}}$  are estimated first as they are needed for estimating  $S_{0,\text{veiling}}$ . Equation (14c) returns the mean value of the four expressions enclosed in square brackets.

The measurement results  $S_{0^\circ}$ ,  $S_{45^\circ}$ ,  $S_{90^\circ}$ , and  $S_{135^\circ}$  are given in Table 2. The first three components of the corresponding estimated Stokes vector of the veiling light  $S_{\text{veiling}}$  are  $S_{0,\text{veiling}} = 759.71$ ,  $S_{1,\text{veiling}} = 187.99$ , and  $S_{2,\text{veiling}} = 41.61$ , calculated by Eq. (14). We then rotated the polarization axis of the mounted linear polarizer to an unknown position and recorded its polarization image  $S_{\text{image}}$  under the same illumination condition. With the estimated  $S_{\text{veiling}}$ , the Stokes vector of this target was retrieved by the following expression, which is the inverse of Eq. (9):

$$S_{\text{target,r}} = (S_{\text{image}} - S_{\text{veiling}}) \times \exp(cL). \quad (15)$$

Here,  $L$  is the length of the water tank, which is 0.5 m. The attenuation coefficient  $c$  of the water in the tank was measured by the ac-s instrument (WET Labs) and was  $3.47 \text{ m}^{-1}$  for the wavelength of 530 nm. In order to test the accuracy of the retrieved target polarization, we also removed the water tank and

**Table 2. Stokes Vector Images of  $0^\circ$ ,  $45^\circ$ ,  $90^\circ$ , and  $135^\circ$  Polarizers When the Water Tank was Removed**

Polarizer	Camera Measurement		
	$S_0$	$S_1$	$S_2$
$0^\circ$	1086.99	549.83	37.39
$45^\circ$	1090.65	180.17	357.02
$90^\circ$	1088.96	-132.18	45.82
$135^\circ$	1084.21	195.82	-272.96

**Table 3. Retrieved Stokes Vector of a Linear Polarizer Whose Polarization Axis Position is Unknown and the Corresponding Measured Stokes Vector of the Same Polarizer When the Water Tank Was Removed**

	$S_0$	$S_1$	$S_2$	DoLP	AoLP
$S_{\text{image}}$	1099.69	135.70	361.37	0.35	$34.71^\circ$
$S_{\text{target,m}}$	2011.74	-353.3	1935.72	0.97	$50.17^\circ$
$S_{\text{target,r}}$	1927.32	-296.2	1811.16	0.95	$49.64^\circ$

recorded the target's polarization image  $S_{\text{target,m}}$ . This measurement was conducted under the illumination conditions similar to the one in Fig. 5(a). All light bulbs in the laboratory including the additional desk lamp were turned off.  $S_{\text{target,r}}$ ,  $S_{\text{target,m}}$ , and  $S_{\text{image}}$  are shown in Table 3. Comparison between  $S_{\text{target,m}}$  and  $S_{\text{image}}$  shows that the turbid water in the tank significantly changes the polarization characteristics of the target's polarization image. However, the agreement between  $S_{\text{target,r}}$  and  $S_{\text{target,m}}$  shows that the target polarization characteristics were successfully retrieved after removing the veiling light estimated through Eq. (14).

**B. Target Polarization Retrieval: Field Experiment**

Having demonstrated the target polarization retrieval method in laboratory conditions, we applied it to retrieve target polarization characteristics from its polarization images acquired in the field experiment in Curacao, July 2012 (Station A), described in Section 4. The target is shown in Fig. 8(b). According to the basic principle of our polarization retrieval method, the first step is to estimate the Stokes vector of the veiling light from polarization images of targets with special polarization states. Therefore, we selected three target elements in the right column, which are  $0^\circ$ ,  $45^\circ$ , and  $90^\circ$  linear polarizers without depolarization film. Although they were attached to a mirror, they still work as polarization filters according to Eq. (13). Then we can use the  $S_1$  component of the pixels corresponding to the  $45^\circ$  polarizer to estimate  $S_{1,\text{veiling}}$  ( $S_{1,\text{veiling}} = S_{1,45^\circ}$ ) and the  $S_2$  component of the pixels corresponding to the  $0^\circ$  and  $90^\circ$  polarizers to estimate  $S_{2,\text{veiling}}$  [Eq. (14b)]. Estimating  $S_{0,\text{veiling}}$  is different from Eq. (14c) because in the field experiment the underwater light field  $S_{\text{water}}$  is partially polarized and then the relationships corresponding to the  $S_0$  component shown in Table 1 are not applicable. However, for the polarimetric images taken in the ocean, the pixels corresponding to the background water also contain useful information. According to Eqs. (11) and (12),  $S_{\text{veiling}}$  is proportional to  $S_{\text{water}}$ :

$$\frac{S_{\text{veiling}}}{S_{\text{water}}} = 1 - \exp(-cL). \quad (16)$$

$S_{\text{water}}$  can be obtained from pixels of the water in the polarization images.  $S_{1,\text{veiling}}$  and  $S_{2,\text{veiling}}$  can be estimated from the pixels corresponding to the  $0^\circ$ ,  $45^\circ$ , and  $90^\circ$  linear polarizers. Equation (16) shows that the attenuation coefficient  $c$  can be retrieved from polarization images if the distance between the target and the camera is known. Then  $S_{0,\text{veiling}}$  can be estimated by the following expression:

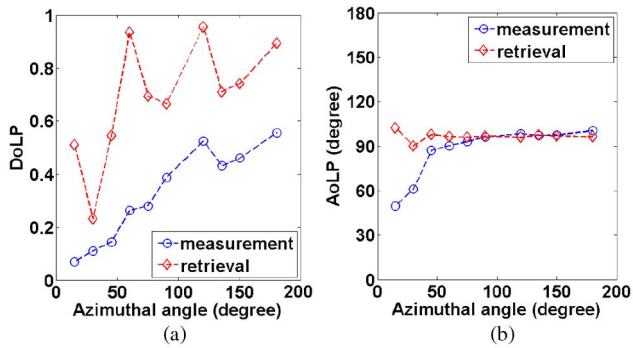


**Fig. 14.** Measured and retrieved (a) DoLP and (b) AoLP of the 90° polarizer. The data for the measured plots are from the pixels of the Stokes vector image corresponding to the 90° polarizer. The data were acquired at Station A.

$$S_{0,\text{veiling}} = S_{0,\text{water}} \times [1 - \exp(-cL)]. \quad (17)$$

We used polarimetric images of the targets obtained at Station A to test our retrieval method. According to Eq. (16), we have three independent estimations of  $1 - \exp(-cL)$ , which are  $\frac{S_{1,45^\circ}}{S_{1,\text{water}}}$ ,  $\frac{S_{2,0^\circ}}{S_{2,\text{water}}}$ , and  $\frac{S_{2,90^\circ}}{S_{2,\text{water}}}$ . After averaging, the estimated  $cL$  is 0.24. Because the distance between the target and the camera is  $L = 1$  m, the estimated attenuation coefficient  $c$  is  $0.24 \text{ m}^{-1}$ . Meanwhile, the value of  $c$  measured by the ac-s instrument (WET Labs) is  $0.21 \text{ m}^{-1}$ . Due to the acceptance angle issue “true”  $c$  value is expected to be 20%–30% higher than measured by ac-s. In any case, taking into account the differences in measurement methodologies the retrieval of  $c$  value can be considered as reasonably accurate. Upon obtaining the estimated  $c$ , we used pixels corresponding to the 0°, 45°, and 90° linear polarizers and the water in the polarization images to estimate  $S_{\text{veiling}}$ . Then the target polarization can be retrieved according to Eq. (15). The retrieved DoLP and AoLP of the 90° polarizer are shown in Fig. 14. It can be seen that except for small azimuthal angles, the average reconstructed DoLP is around 0.8 and the reconstructed AoLP is close to 90°, i.e., the polarization axis of the 90° polarizer. The small difference between the measured AoLP and the retrieved AoLP at several azimuthal angles suggests that the veiling light contribution to the measured Stokes vector and specifically to the measured  $S_1$  and  $S_2$  components was small. Therefore, the main effect of veiling light removal is the increase of the DoLP. These results show that our retrieval method generally works for the 90° polarizer. However, the polarization retrieval of the 0° and 45° polarizers by the same method was more problematic due to the additional flaws of the target elements, which made polarized fields from them more complex and complicated the retrieval.

## 6. CONCLUSIONS

In this paper, we analyzed polarization fields from the objects in an underwater environment using several simulation and experimental approaches in the lab and in the field. We first elaborated on the concept of polarized BSF used for polarized light. Through both Monte Carlo simulations and laboratory experiment of the polarized BSF in underwater environments, we

obtained a simplified underwater polarimetric imaging model, and then analyzed polarimetric images of a manmade underwater target with known polarization properties, which were acquired by a full Stokes vector imaging camera in a field experiment. With the knowledge acquired in the analysis of such a forward polarimetric imaging process, we explored a method to retrieve both the inherent optical properties of the water and the polarization characteristics of the target. The method has been demonstrated by both laboratory and field experiments.

In general, analysis of an underwater target’s polarimetric images and the inverse process polarization retrieval are complicated. As shown in the paper, even in the case of clear water, the retrieved DoLP of the 90° polarizer is not equal to 1, suggesting that other factors that induce polarization change are not considered. For example, the impact of possible glare on the polarizer was not included in the model but may alter the measured polarization of the target used in the field experiment. In addition, it is worth noting that the work presented in this paper is based on the assumption of a turbid ocean. The real underwater environment is both turbid and turbulent. Oceanic turbulence blurs the image of an underwater target [44] and alters the polarization properties of a propagating optical beam [45]. Much work needs to be done to reveal the underlying physics of light propagation in the ocean and the associated polarization changes. Such understanding will be helpful for purposes of target camouflage or, conversely, for better detection and imaging of partially polarized targets in an underwater environment.

**Funding.** Office of Naval Research (ONR) (N000140911054); National Science Foundation (NSF) (OCE-1130906); National Aeronautics and Space Administration (NASA) (NNX13AF44G); National Oceanic and Atmospheric Administration (NOAA) (NA11SEC4810004).

**Acknowledgment.** We are grateful to the anonymous reviewer for helpful suggestions, which improved the quality of the paper.

## REFERENCES

1. G. W. Kattawar, “Genesis and evolution of polarization of light in the ocean [Invited],” *Appl. Opt.* **52**, 940–948 (2013).
2. N. W. Roberts, M. L. Porter, and T. W. Cronin, “The molecular basis of mechanisms underlying polarization vision,” *Phil. Trans. R. Soc. B* **366**, 627–637 (2011).
3. M. Kamermans and C. Hawryshyn, “Teleost polarization vision: how it might work and what it might be good for,” *Phil. Trans. R. Soc. B* **366**, 742–756 (2011).
4. G. M. Calabrese, P. C. Brady, V. Gruev, and M. E. Cummings, “Polarization signaling in swordtails alters female mate preference,” *Proc. Natl. Acad. Sci. USA* **111**, 13397–13402 (2014).
5. S. Johnsen, “Hide and seek in the open ocean: pelagic camouflage and visual countermeasures,” *Annu. Rev. Mar. Sci.* **6**, 369–392 (2014).
6. P. C. Brady, K. A. Travis, T. Maginnis, and M. E. Cummings, “Polarocryptic mirror of the lookdown as a biological model for open ocean camouflage,” *Proc. Natl. Acad. Sci. USA* **110**, 9764–9769 (2013).
7. P. C. Brady, A. A. Gilerson, G. W. Kattawar, J. M. Sullivan, M. S. Twardowski, H. M. Dierssen, M. Gao, K. Travis, R. I. Etheredge, A. Tonizzo, A. Ibrahim, C. Carrizo, Y. Gu, B. J. Russell, K. Misliński, S. Zhao, and M. E. Cummings, “Open-ocean fish reveal an omnidirectional solution to camouflage in polarized environments,” *Science* **350**, 965–969 (2015).

8. S. Zhao, P. C. Brady, M. Gao, R. I. Etheredge, G. W. Kattawar, and M. E. Cummings, "Broadband and polarization reflectors in the look-down, Selene vomer," *J. R. Soc. Interface* **12**, 20141390 (2015).
9. J. Olson, A. Manjavacas, L. Liu, W. Chang, B. Foerster, N. S. King, M. W. Knight, P. Nordlander, N. J. Halas, and S. Link, "Vivid, full-color aluminum plasmonic pixels," *Proc. Natl. Acad. Sci. USA* **111**, 14348–14353 (2014).
10. J. S. Jaffe, "Computer modeling and the design of optimal underwater imaging systems," *IEEE J. Ocean. Eng.* **15**, 101–111 (1990).
11. P. C. Y. Chang, J. C. Flitton, K. I. Hopcraft, E. Jakeman, D. L. Jordan, and J. G. Walker, "Improving visibility depth in passive underwater imaging by use of polarization," *Appl. Opt.* **42**, 2794–2803 (2003).
12. Y. Y. Schechner and N. Karpel, "Recovery of underwater visibility and structure by polarization analysis," *IEEE J. Ocean. Eng.* **30**, 570–587 (2005).
13. M. Dubreuil, P. Delrot, I. Leonard, A. Alfalou, C. Brosseau, and A. Dogariu, "Exploring underwater target detection by imaging polarimetry and correlation techniques," *Appl. Opt.* **52**, 997–1005 (2013).
14. L. E. Mertens and J. F. S. Replogle, "Use of point spread and beam spread function for analysis of imaging systems in water," *J. Opt. Soc. Am.* **67**, 1105–1117 (1977).
15. H. R. Gordon, "Equivalence of the point and beam spread functions of scattering media: a formal demonstration," *Appl. Opt.* **33**, 1120–1122 (1994).
16. S. Q. Duntley, "Underwater lighting by submerged lasers and incandescent sources," *Tech. Rep.* (Scripts Institution of Oceanography, University of California, 1971).
17. K. J. Voss, "Simple empirical model of the oceanic point spread function," *Appl. Opt.* **30**, 2647–2651 (1991).
18. L. S. Dolin, G. D. Gilbert, I. Levin, and A. Luchinin, *Theory of Imaging Through Wavy Sea Surface* (Russian Academy of Sciences Institute of Applied Physics, 2006).
19. W. Hou, D. J. Gray, A. D. Weidemann, and R. A. Arnone, "Comparison and validation of point spread models for imaging in natural waters," *Opt. Express* **16**, 9958–9965 (2008).
20. Z. Xu and D. K. P. Yue, "Analytical solution of beam spread function for ocean light radiative transfer," *Opt. Express* **23**, 17966–17978 (2015).
21. M. Vedel, S. Breugnot, and N. Lechocinski, "Full Stokes polarization imaging camera," *Proc. SPIE* **8160**, 81600X (2011).
22. D. Goldstein, *Polarized Light*, 2nd ed. (CRC Press, 2007).
23. J. M. Sullivan and M. S. Twardowski, "Angular shape of the oceanic particulate volume scattering function in the backward direction," *Appl. Opt.* **48**, 6811–6819 (2009).
24. H. H. Tynes, G. W. Kattawar, E. P. Zege, I. L. Katsev, A. S. Prikhach, and L. I. Chaikovskaya, "Monte Carlo and multicomponent approximation methods for vector radiative transfer by use of effective Mueller matrix calculations," *Appl. Opt.* **40**, 400–412 (2001).
25. A. A. Gilerson, J. Stepinski, A. I. Ibrahim, Y. You, J. M. Sullivan, M. S. Twardowski, H. M. Dierssen, B. Russell, M. E. Cummings, P. Brady, S. A. Ahmed, and G. W. Kattawar, "Benthic effects on the polarization of light in shallow waters," *Appl. Opt.* **52**, 8685–8705 (2013).
26. D. J. Gray, "Order-of-scattering point spread and modulation transfer functions for natural waters," *Appl. Opt.* **51**, 6753–6764 (2012).
27. G. W. Kattawar, G. N. Plass, and J. A. Guinn, Jr., "Monte Carlo calculations of the polarization of radiation in the Earth's atmosphere-ocean system," *J. Phys. Oceanogr.* **3**, 353–372 (1973).
28. D. J. Gray, personal communications.
29. M. I. Mishchenko, L. D. Travis, and A. A. Lacis, *Scattering, Absorption, and Emission of Light by Small Particles* (Cambridge University, 2002).
30. J. S. Tyo, D. L. Goldstein, D. B. Chenault, and J. A. Shaw, "Review of passive imaging polarimetry for remote sensing applications," *Appl. Opt.* **45**, 5453–5469 (2006).
31. H. G. Akarçay, A. Hohmann, A. Kienle, M. Frenz, and J. Ricka, "Monte Carlo modeling of polarized light propagation: Stokes vs. Jones. Part I," *Appl. Opt.* **53**, 7576–7585 (2014).
32. E. P. Zege, A. P. Ivanov, and I. L. Katsev, *Image Transfer through a Scattering Medium* (Springer-Verlag, 1991).
33. R. A. Leathers, T. Downes, C. O. Davis, and C. D. Mobley, "Monte Carlo radiative transfer simulations for ocean optics: A practical guide," *Tech. Rep.* (Naval Research Laboratory, 2004).
34. J. C. Ramella-Roman, S. A. Prahl, and S. L. Jacques, "Three Monte Carlo programs of polarized light transport into scattering media: Part I," *Opt. Express* **13**, 4420–4438 (2005).
35. K. J. Voss and E. S. Fry, "Measurement of the Mueller matrix for ocean water," *Appl. Opt.* **23**, 4427–4439 (1984).
36. C. D. Mobley, *Light and Water Radiative Transfer in Natural Waters* (Academic, 1994).
37. C. D. Mobley, *HydroPol Mathematical Documentation* (Sequoia Scientific, 2014).
38. B. M. Cochenour, L. J. Mullen, and A. E. Laux, "Characterization of the beam-spread function for underwater wireless optical communications links," *IEEE J. Ocean. Eng.* **33**, 513–521 (2008).
39. J. Fade, S. Panigrahi, A. Carré, L. Frein, C. Hamel, F. Bretenaker, H. Ramachandran, and M. Alouini, "Long-range polarimetric imaging through fog," *Appl. Opt.* **53**, 3854–3865 (2014).
40. B. Cochenour, L. Mullen, and J. Muth, "Effect of scattering albedo on attenuation and polarization of light underwater," *Opt. Lett.* **35**, 2088–2090 (2010).
41. W. Cox and J. Muth, "Simulating channel losses in an underwater optical communication system," *J. Opt. Soc. Am. A* **31**, 920–934 (2014).
42. A. Tonizzo, J. Zhou, A. Gilerson, M. S. Twardowski, D. J. Gray, R. A. Arnone, B. M. Gross, F. Moshary, and S. A. Ahmed, "Polarized light in coastal waters: hyperspectral and multiangular analysis," *Opt. Express* **17**, 5666–5683 (2009).
43. Y. You, A. Tonizzo, A. A. Gilerson, M. E. Cummings, P. Brady, J. M. Sullivan, M. S. Twardowski, H. M. Dierssen, S. A. Ahmed, and G. W. Kattawar, "Measurements and simulations of polarization states of underwater light in clear oceanic waters," *Appl. Opt.* **50**, 4873–4893 (2011).
44. W. Hou, S. Woods, E. Jarosz, W. Goode, and A. Wedieman, "Optical turbulence on underwater image degradation in natural environments," *Appl. Opt.* **51**, 2678–2686 (2012).
45. O. Korotkova and N. Farwell, "Effect of oceanic turbulence on polarization of stochastic beams," *Opt. Commun.* **284**, 1740–1746 (2011).